

Simultaneous Observations of Surface Layer Profiles of Humidity, Temperature, and Wind using Scanning Lidar Instruments

Florian Späth¹, Andreas Behrendt¹, W. Alan Brewer², Diego Lange¹, Christoph Senff^{2,3}, David D. Turner⁴, Timothy J. Wagner⁵, Volker Wulfmeyer¹

¹University of Hohenheim, Institute of Physics and Meteorology, Garbenstr. 30, 70599 Stuttgart, Germany

²NOAA / OAR / Chemical Sciences Laboratory, Boulder, CO, USA

³Cooperative Institute for Research in the Environmental Sciences, University of Colorado, Boulder, CO, USA

⁴NOAA/OAR/Global Systems Laboratory, Boulder, Colorado, USA

⁵Space Science and Engineering Center, University of Wisconsin–Madison, Madison, Wisconsin, USA

Corresponding author: Florian Späth (f.spaeth@uni-hohenheim.de)

Key Points:

- Surface layer profiles observed simultaneously with scanning Doppler, water vapor differential absorption and temperature rotational Raman lidar
- Comparison of Monin-Obukhov similarity theory profiles with lidar profiles
- Demonstration of method to estimate friction velocity as well as latent and sensible surface heat fluxes from fits to the lidar surface layer profiles

This article has been accepted for publication and undergone full peer review but has not been through the copyediting, typesetting, pagination and proofreading process, which may lead to differences between this version and the [Version of Record](#). Please cite this article as [doi: 10.1029/2021JD035697](https://doi.org/10.1029/2021JD035697).

This article is protected by copyright. All rights reserved.

Abstract

We demonstrate the combination of three Doppler lidars, a water vapor differential absorption lidar and a temperature rotational Raman lidar for the investigation of the interactions between the land-surface and the atmospheric boundary layer. This combination of scanning lidars was operated for the first time during the Land-Atmosphere Feedback Experiment (LAFE) at the Atmospheric Radiation Measurement program's Southern Great Plain site, Oklahoma, USA, in August 2017, and provided simultaneous surface layer profiles of horizontal wind, humidity and temperature. The horizontal wind profiles were determined using the dual-Doppler method with two Doppler lidars. The scans were performed above four towers providing atmospheric variables and fluxes. These combined lidar data allowed for the estimation of the friction velocity as well as the surface latent and sensible heat fluxes. For this purpose, profiles calculated with Monin-Obukhov similarity theory (MOST) were fitted with the Levenberg-Marquardt nonlinear least square curve-fitting method to the measured surface-layer lidar profiles. We present case studies of three 50-minute periods to illustrate the new method. The measurements resulted in friction velocities of 0.31, 0.29, and 0.38 ms^{-1} , sensible surface heat fluxes of 312.1, 234.1, and 183.3 Wm^{-2} and latent surface heat fluxes of 251.8, 227.3, and 274.4 Wm^{-2} . These values were compared with the in-situ measurements of the towers. Considering the sampling differences and the error analyses, the results agree within 25.1 %, 42.5 %, and 28.8 %, respectively, demonstrating that this synergy of scanning active remote sensing systems can be used to derive surface fluxes with reasonable accuracy.

1 Introduction

The development of the planetary boundary layer (PBL) is related to the exchange of momentum, energy, and water between the atmosphere and the land surface as well as to the resulting feedback processes in the land-atmosphere (L-A) system (Santanello et al., 2018). The representation and the parametrization of surface fluxes in models is crucial in weather and climate models for reliable forecasts and simulations. The surface layer (SL) is the direct connection between the land-surface and the atmosphere. The behavior of surface layer profiles depends on the vertical stability in the atmosphere as well as the soil and the land cover properties and their heterogeneities.

In order to describe the dependence of SL profiles on the surface fluxes, flux-gradient relationships have been developed. These relationships are fundamental for the parameterization of fluxes in weather forecast, climate and earth system models. The most prominent and widely used scheme is the Monin-Obukhov similarity theory (MOST) (e.g., Monin and Obukhov, 1954; Obukhov, 1971). It relates the vertical gradients of wind, potential temperature and specific humidity in the SL to fluxes of momentum, heat and moisture in combination with dimensionless similarity functions. These similarity functions depend on the atmospheric stability and are typically classified by the bulk Richardson number R_b . The height z above the canopy is scaled with the Monin-Obukhov length L . MOST is used for the parameterization of surface turbulent fluxes in almost all weather forecast and climate models such as in the SL scheme of the Weather Research and Forecast (WRF) model (Jiménez et al., 2012).

However, MOST is not the only option for the description of flux-gradient relationships in the SL. Another approach relates the fluxes and the gradients in a similar way as in MOST but uses a similarity function, which is dependent on R_b (Lee and Buban, 2020). With increasing numbers and different kinds of observations, machine learning (ML) may be another method to identify L-A relationships and to develop new parameterizations of the SL processes based on observations. ML has already been applied to evaluate parameterizations in numerical weather prediction models (Bodini et al., 2020), to emulate computationally expensive parameterizations more efficiently (Lagerquist et al., 2021), and to transfer parameterizations of small scale processes for larger scales in climate models (Yuval and O’Gorman, 2020) and is one objective of the CHEESEHEAD19 study (Chequamegon Heterogeneous Ecosystem Energy-Balance Study Enabled by a High-Density Extensive Array of Detectors 2019) for model-data comparisons (Butterworth et al., 2021).

Measurements of fluxes are usually performed with the eddy covariance (EC) technique (Lee et al. 2004, Mauder et al. 2020) using in-situ sensors located 2 m above the canopy (Foken, Wizemann et al. 2015, Kiese et al. 2018). Gradient and further flux measurements are made with additional sensors located at approx. 10 m above the canopy (Lee et al. 2019, Lee and Buban 2020). Further insight in SL profiles and gradients have been achieved with sensors at different levels at high towers such as at the German Weather Service Lindenberg Meteorological Observatory - Richard Assmann Observatory (Neisser et al., 2002), the Boulder tower (Wolfe and Lataitis, 2018), the WLEF-TV tower in Wisconsin (Berger et al., 2001), the tower in

Cabauw (Röckmann et al., 2016), and the Amazon Tall Tower Observatory (Andreae et al., 2015).

There are a number of conditions that must be fulfilled so that SL schemes like MOST can be applied. This includes a homogeneous land surface and quasi-stationary conditions (with respect to incoming radiation, surface fluxes and the soil, land cover, and atmospheric conditions). Also, it is expected that the height dependence of the fluxes can be neglected; the SL is then a constant flux layer. The SL schemes are only dependent on surface scaling parameters so that it is assumed that the fluctuations in the variables determining the fluxes are not influenced by entrainment processes at the top of the PBL.

However, the land surface is generally heterogeneous. On the one hand, this is due to the horizontal variability of soil properties such as the soil texture or soil variables like soil moisture. On the other hand, it is due to the heterogeneity of the land cover. In order to study a larger area and to investigate the influence and applicability of MOST in heterogeneous terrain, spatially-resolved observations of the land surface and the atmosphere above are required. The land surface can be observed with remote sensing systems from aircraft or satellites. Measurements of atmospheric variables with high temporal and spatial resolutions are even more challenging. These must provide fields of wind, temperature, and moisture at the same time, as these variables are entangled in all standard SL schemes. Recently, a synergy of scanning wind, temperature and water-vapor lidar systems became available fulfilling these measurement needs. These are based on coherent Doppler lidar (DL) systems for high-resolution line-of-sight (LOS) wind measurements (Choukulkar et al., 2017). The temperature rotational Raman lidar (TRL) provides the required range-resolved temperature measurements (Hammann et al., 2015; Behrendt et al., 2015; Behrendt et al., 2020) and either a water-vapor Raman lidar (WVRL) (Wulfmeyer et al., 2010; Turner et al., 2002) or a water-vapor differential absorption lidar (WVDIAL) produce the necessary measurements of the moisture field (Wulfmeyer, 1999; Wulfmeyer et al., 2016; Muppa et al., 2016; Späth et al., 2016).

With this combination of DL, TRL, and WVDIAL, observations of the SL down to the canopy top can be obtained with a suitable scan strategy. Past studies have observed SL moisture profiles from lidar using a solar blind WVRL approach (Eichinger et al., 2000; Froidevaux et al., 2013) and with WVDIAL (Späth et al. 2016). Range-height indicator (RHI) scans can be used to

derive virtual tower profiles of temperature and moisture in dependence of range. The determination of horizontal wind profiles requires at least two DLs using the crossing of two RHI scans from two different directions. Validation of this technique has been demonstrated in Calhoun et al. (2006) and Choukulkar et al. (2017). Temperature profiles with sufficient spatial-temporal resolutions of a few seconds and a few tens of meters have been presented in Hammann et al. (2015), Behrendt et al. (2015), and Behrendt et al. (2020); however, with the exception of a few elevation scans with coarse resolution (Radlach et al, 2008; Hammann et al., 2015), scanning lidar temperature profiles in the SL have not yet been described in the literature. Other temperature profiling techniques like passive remote sensing with microwave radiometer temperature profilers or spectral infrared profilers do not achieve the required vertical resolution in the SL as they have too few degrees of information for signal (Turner and Löhnert, 2021; Blumberg et al., 2015).

This situation changed in August 2017, when the Land-Atmosphere Feedback Experiment (LAFE, Wulfmeyer et al., 2018) was performed at the Atmospheric Radiation Measurements (ARM) Program's Southern Great Plain (SGP) site (Sisterson et al., 2016) in Oklahoma, USA (36.607 N, 97.488 W, 314-m msl). Here, a novel scanning lidar synergy was deployed consisting of a combination of DLs, TRL, and WVDIAL. The goal of LAFE was to demonstrate the capabilities of these instruments to resolve profiles of atmospheric variables in the SL and to perform high-resolution measurements in the vertically staring mode. With specific scan configurations, it was possible to observe the atmosphere from the surface into the lower troposphere with high vertical resolution in the SL and in the PBL nearly simultaneously. By combining these profiles, further quantities like surface sensible and latent heat fluxes can be derived and turbulent to mesoscale structures can be detected.

In this manuscript we introduce our new methodology to simultaneously derive wind, temperature, and moisture profiles in the SL. In Sect. 2, the measurement setup of LAFE and a brief instrument description is given. The methodology is described in Sect. 3 which will be applied to the derived lidar profiles presented in Sect. 4. The flux estimation from the lidar profile is shown and discussed in Sect. 5. Finally, we provide a summary and an outlook.

2 The Land Atmosphere Feedback Experiment (LAFE)

2.1 LAFE goals and instrumental setup

The Land-Atmosphere Feedback Experiment (LAFE, Wulfmeyer et al., 2018) was initiated in order to study L-A feedback and corresponding key processes in the heterogeneous terrain with different agricultural fields around the ARM SGP site. The campaign was performed during August 2017 with deployment of several instruments to augment the existing ARM observations. The LAFE dataset aims to investigate four research goals (see Wulfmeyer et al., 2018) of which we target Goal 2: map surface momentum, sensible heat, and latent heat fluxes using a synergy of scanning wind, humidity, and temperature lidar systems.

To target this research topic, a novel scanning lidar synergy was realized during LAFE. A combination of a WVDIAL, a TRL, and three wind DLs was deployed to measure humidity, temperature, and the horizontal wind velocity in the SL, i.e. the lowest 100 m above the land surface. With specific temporally coordinated scans, two-dimensional fields of wind, humidity and temperature were captured.

The setup during LAFE contained five lidar systems (Figure 1): one WVDIAL, one TRL, both from University of Hohenheim (UHOH), one Leosphere 200S® DL (DALEK) from NOAA CSL, and two Halo Streamline XR DLs, one of SPARC (Space Science and Engineering Center (SSEC) Portable Atmospheric Research Center) of SSEC University of Wisconsin and one of CLAMPS (Collaborative Lower Atmospheric Mobile Profiling System) of NOAA NSSL and the University of Oklahoma. Complete details about CLAMPS and SPARC are available in Wagner et al., (2019). The WVDIAL, the TRL, and DALEK were located at the north-east corner of the ARM SGP central facility (CF) and performed vertical scans along the main LAFE scan axis (red line in Figure 1), extending to the northeast. The two DLs from SPARC and CLAMPS were placed north and east of the main scan axis to perform cross-scans for doing Dual-Doppler (SPARC green lines, CLAMPS blue lines in Figure 1). By this means, four virtual towers along the main scan direction were realized at positions where energy balance closure (EB) stations were setup at the land-surface (Temple et al., 2019). While the WVDIAL, the TRL and DALEK scanned continuously along the main axis, the SPARC and CLAMPS DLs scanned periodically over the EB towers 1, 2 and 2, 3, 4 (TWR 1-4), respectively. The setup is presented in Figure 1 and the operating parameters of all lidars are listed in Table 1. The land cover at the EB stations

was a mixture of grassland and soybeans at TWR 1, native grassland at TWR 2, mature soybeans at TWR 3, and pasture at TWR 4 (Wulfmeyer et al., 2018; Lee and Buban, 2020).

During the campaign period August 2017, the SL measurements were organized in intensive observations periods (IOPs). Here we present measurements from IOP 11 on 23 August 2017. On this day, a high-pressure system was located over northern Oklahoma resulting in clear sky conditions over most of the measurement area throughout the day. Only the southern portion of the measurement area (over 50 kilometers away) had a band of clouds, which slowly dissipated throughout the day. The IOP started at 1230 CDT (1730 UTC) when the convective boundary layer was developed and lasted through the night time transition until 2240 CDT (0340 UTC). The scanning lidars performed repeated vertical range-height indicator (RHI) scans in an hourly cycle: capture SL profiles for 50 minutes each hour (starting at minute 40 of each hour through minute 30 of the next hour) and then observe the full extent of the PBL up to the lower troposphere for the remaining 10 minutes. We designed the scan pattern (e.g. scan speed, scan range, averaging period, accumulation time) to achieve errors which are low enough that the gradients in the SL can be resolved. For the wind measurements the uncertainty is $\sim 0.2 \text{ ms}^{-1}$, for humidity $\sim 0.12 \text{ gm}^{-3}$, and for temperature $\sim 1 \text{ K}$. To determine the uncertainties of wind measurements we performed comparisons with 10 m tower measurements (Choukulkar et al., 2017) and for determination of the uncertainties of the humidity and temperature profiles we used the noise variance of high-resolution data (Lenschow et al, 2000; Wulfmeyer et al., 2016) and scaled the uncertainty to the resulting temporal and spatial resolution of the mean profile (Ismail and Browell, 1989; Späth et al., 2016). The vertical resolution of the lidar measurements was limited by two factors: 1) the elevation scan speed combined with the temporal resolution of the measurements (see Table 1) and 2) the vertical projection of the gate width. Further details are discussed in the Appendix. The CBL top on this day was around 1000 m. The temperature reached up to $25 \text{ }^\circ\text{C}$ with relative humidity of around 40 %. Wind were light, at 5 ms^{-1} from the east. The daily maximum surface latent and sensible heat fluxes at the ARM SGP CF were up to 350 Wm^{-2} and 170 Wm^{-2} , respectively. At towers 1, 2, and 3 the maximum latent and sensible heat fluxes for this day were both similar with $\sim 220 \text{ Wm}^{-2}$.

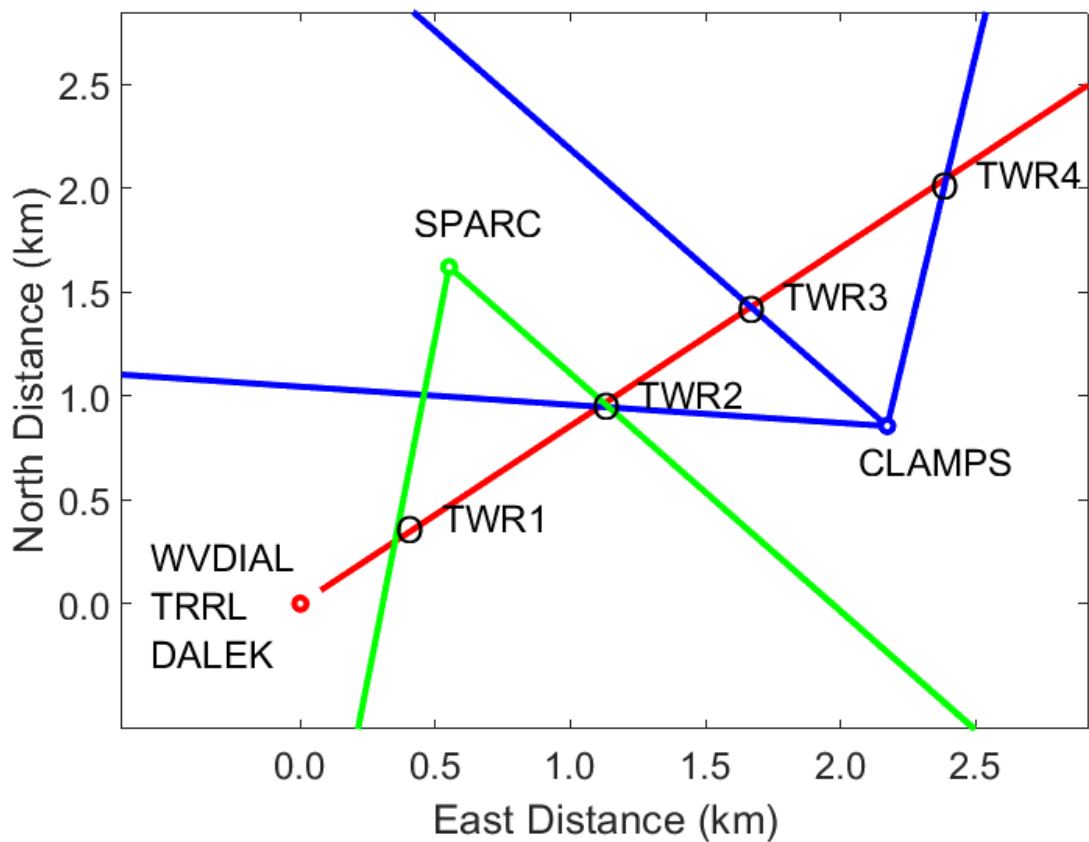


Figure 1 A plan view of the LAFE virtual tower layout. The UHOH and NOAA scanning lidars were located at the ARM SGP central facility and performed RHI scans in the north-east direction (red line). The location of the two cross-scanning Doppler lidars and their RHI scan planes are shown: SPARC (green) and CLAMPS (blue). The virtual towers are labeled TWR1-4 where EB stations were placed at the land surface. Distances between the lidars and EB stations are given in Table 1

Table 1 Operating parameters for the scanning lidars. The 200S is manufactured by Leosphere and the HALO units are Streamline XRs manufactured by Halo Photonics. The table shows the data acquisition (DAQ) rate, gate length, angular velocity for each lidar at each tower and the corresponding distance.

		DAQ rate	Gate length	Angular velocity (deg s ⁻¹)				Distance to Tower (m)			
		(Hz)	(m)	T1	T2	T3	T4	T1	T2	T3	T4
WVDIAL		10	15	0.1				540	1480	2200	3120
TRL		1	7.5	0.2				540	1480	2200	3120
DALEK	200S	2	50	0.08				540	1480	2200	3120
CLAMPS	HALO	2	60	-	0.33	0.46	0.30	1830	1040	750	1180
SPARC	HALO	0.66	60	0.09	0.11	-	-	1280	890	1140	1880

2.2 Doppler Wind Lidar (DL)

Three scanning DLs were used in the LAFE setup to perform low angle elevation RHI scans that intersected over four locations, forming virtual towers. The virtual tower locations were positioned over EB stations located at the center of an area of different land usage types. Figure 1 shows the layout of the lidars, EB stations (TWR 1-4) and RHI scan planes and Table 1 shows the type of lidars and operating parameters for each system.

Following the uncoordinated virtual tower scan design described in Choukulkar et al. (2017), a repeating 67 second scan sequence was designed for each lidar. DALEK performed a slow RHI in the primary measurement plane (that shared with the EB stations, WVDIAL and TRL), while SPARC and CLAMPS performed RHIs in multiple planes intersecting the main plane during the same time period. The CLAMPS 67 second sequence included RHIs in three planes, covering TWR 2-4 and a 9 second period staring vertically. Originally, SPARC was to have covered TWR 1-3, but poor system sensitivity mandated accumulating more pulses and scanning slower to provide measurements at the range of the towers. This resulted in SPARC only scanning two planes (TWR 1 & 2) and doing so at a rate where the entire sequence took two 67 s time periods. All scans were optimized to provide coverage for virtual towers of 100 m height.

The virtual tower analysis utilized a capture area of $\pm 100\text{m}$ around the tower in the north and east directions and height range of 2 m. All LOS data whose gate centers fell within the 200 m x 200 m x 2 m volume and acquisition times fell within the same prescribed averaging time window were used to derive the horizontal wind vector (Choukulkar et al., 2017). While the analysis was performed using 2 m vertical binning, the operational configuration of the HALO lidars (CLAMPS and SPARC) dominated the vertical resolution of the virtual tower horizontal wind speed measurement because of their placement relative to the main scan plane, longer processing gate width and the need to scan more quickly in order to cover multiple scan planes. Nevertheless, for lower heights the vertical resolution above all towers was 3 m. The resolution increased linearly at TWR 1 above 45 m from 3 m to 5.2 m at 100 m agl, at TWR 2 above 50 m from 3 m to 6.2 m at 100 m agl, at TWR 3 above 40 m from 3 m to 7.5 m at 100 m agl, and at TWR 4 above 60 m from 3 m to 4.9 m at 100 m agl.

The virtual tower horizontal wind profiles were processed with two different temporal windows: 6-minutes and 48-minutes. The 48-minutes data have the same averaging time window as the WVDIAL and TRL profiles. The 6-minute processing window was used to estimate atmospheric variability over the 48-minutes period. The standard deviation of the 6-minute results were used to calculate the error bars of the 48-minutes mean wind profile. There is a gap at 15 m in all profiles which was caused by power line blockage of the DALEK beam in the main plane. This lidar's results are common to all retrievals and cause a gap when not available.

2.3 Water Vapor Differential Absorption Lidar (WVDIAL)

High-resolution water vapor measurements were performed with the WVDIAL of University of Hohenheim (UHOH) (Wagner et al., 2013; Späth et al., 2013; Muppa et al., 2016; Späth et al. 2016). The DIAL technique uses two wavelengths and the spectral properties of WV to show high absorption at one of the wavelengths and low absorption at the other wavelength. The UHOH WVDIAL generates laser pulses at 818 nm with a repetition rate of 300 Hz alternating between the two wavelengths. Details of the high-power laser transmitter are presented in Metzendorf (2018). Maximum output power is 10 W, which can be transmitted via a free beam into the atmosphere for vertical pointing measurements. For scanning operation, the laser pulses are transmitted via a transmitting telescope, which is mounted to the scanner. For this operation mode the laser output power is limited due to the use of an optical fiber as flexible guide medium for the laser pulses to the transmitting telescope. The scanner is capable to direct to the full upper hemisphere and holds the receiving telescope with 80-cm primary mirror and the 20-cm primary mirror of the transmitting telescope in biaxial configuration. An avalanche photo diode is used for detection of the elastic backscatter signal with a spatial resolution of 15 m. The recorded raw signal is averaged to a temporal resolution of 0.1 s. A detailed description of the UHOH WVDIAL setup and analysis procedure is given in Späth et al. (2016).

During LAFE, the WVDIAL performed repeated RHI scans over an angle range of 7° moving consecutively up and downwards with a scan speed of $0.1^\circ/\text{s}$ resulting in a time duration of 70 seconds for each RHI scan. The recorded backscatter signals (raw data) needed to be corrected for an elevation angle offset, a hysteresis effect caused through the heavy scanner and filtered for disturbing hard target returns due to negative elevation angles and hitting the ground

and other obstacles. The corrected backscatter data were averaged over 1 s and water vapor was calculated with a Savitzky-Golay (SaGo) window of 435 m. For the mean scan of the 50-minute period, data of 42 RHI scans were averaged with a gliding average of 0.2° angle range per profile. Virtual tower profiles can be extracted at distances between 500 m and 2500 m to the lidar. The vertical resolution of the virtual tower profile is defined by the angle resolution and the distance of the profile, e.g., at TWR 2 it resulted in a 3 m vertical resolution.

The statistical uncertainties can be calculated from the time series of the data points of the consecutive scans applying autocovariance function (Späth et al, 2016). In this analysis we show only the uncertainty of the mean profile as error bars.

2.4 Temperature Rotational Raman Lidar (TRRL)

Rotational Raman lidar makes use of the inelastic scattered Raman signals of atmospheric molecules (mainly N_2 and O_2) of different temperature dependency (Cooney, 1972; Behrendt, 2005). From the ratio of the atmospheric backscatter signals, a measurement signal is obtained which depends on atmospheric temperature. The rotational Raman lidar of UHOH aims at high-resolution measurements in the atmospheric boundary layer and lower free troposphere during daytime (Radlach et al., 2008; Hammann et al., 2015; Hammann and Behrendt, 2015). Laser pulses at 355 nm are transmitted into the atmosphere with an average power of around 10 W at a repetition rate of 50 Hz. The beam is directed through the beam steering unit in coaxial configuration with the receiving telescope. The two-mirror beam-steering unit enables us to direct the beam to any azimuth and elevation angle of interest. The receiving telescope is of the Ritchey–Chrétien–Cassegrain type. Its primary mirror has a diameter of 40 cm. To reduce the daylight background, the focused signal passes through a pinhole with selectable diameter. The diameter was set to 3 mm during the LAFe campaign, which results in a full field of view of 0.75 mrad. After passing this field stop, the light is collimated with a lens and then separated with a high-efficient polychromator in different wavelengths to record signals in four channels (elastic, two rotational Raman, water vapor Raman). The signals are detected with photomultiplier tubes and recorded in both analog and photon counting mode with raw-data resolutions of 1 s and 7.5 m.

The scan patterns were coordinated with the UHOH DIAL. Synchronously, low elevation scans were made for 50 min of each hour. These low elevation RHI scans were realized in step and stare mode moving the scanner unit always upwards in steps of 0.1° over an angle range of 7° .

For the data presented here, only the analog data were used because of the large signal intensities in the range of interest of LAFE. After background subtraction the signals of each direction were averaged in time over the 50-minute period and in range with a gliding average of 97.5 m. Then the ratio of the two RR signals was calculated and the calibration was applied to obtain temperature data. For calibration, ten-minute data between the RHI scans were collected in vertical mode and compared with local radiosondes. The potential temperature was calculated from the retrieved temperature using the surface pressure measured at the EB station and extrapolated with a constant pressure laps rate of -0.125 hPa/m. The radial RHI temperature data were finally gridded to a Cartesian coordinate system in order to get virtual towers. The vertical resolution of this Cartesian coordinate system was 5 m while we averaged the data horizontally over 1000 m to reduce the noise and to get representative values for the dimensions of the fields in the region. The statistical uncertainties of these gridded data were estimated with time series of vertical data and higher-order moment analyses (Behrendt et al., 2015; Lange et al., 2019)

3 Methodology

MOST describes the relation between surface momentum and heat fluxes and the gradients of wind, temperature, and humidity with dimensionless similarity functions.

$$\frac{\partial \bar{U}}{\partial z} = \frac{u_*}{k z} \phi_m\left(\frac{z}{L}\right) \quad (1)$$

$$\frac{\partial \bar{\theta}}{\partial z} = \frac{H_0}{u_* k z} \phi_h\left(\frac{z}{L}\right) \quad (2)$$

$$\frac{\partial \bar{q}}{\partial z} = \frac{Q_0}{u_* k z} \phi_q\left(\frac{z}{L}\right) \quad (3)$$

with \bar{U} , $\bar{\theta}$, and \bar{q} being mean wind, potential temperature, and specific humidity, u_* the friction velocity, k the von-Karman constant, H_0 and Q_0 the sensible and latent surface heat fluxes. ϕ_m ,

ϕ_h , and ϕ_q are the similarity functions for momentum, heat, and moisture, respectively, and depend on the ratio of the height z and the Monin-Obukhov length

$$L = -\frac{\overline{\theta_v} u_*^3}{k g \frac{H_0}{\rho c_p}} \quad (4)$$

with θ_v the virtual potential temperature, g the gravitational acceleration, ρ the air density, and c_p the heat capacity at constant pressure.

To evaluate the similarity functions in Eq. (1)-(3) with observations, measurements of the gradients of \bar{U} , $\bar{\theta}$, and \bar{q} are required. Lidar observations provide direct measurements of the profiles of \bar{U} , \bar{T} , and \bar{q} . It is straightforward then to derive $\bar{\theta}$ from \bar{T} in the SL. We will evaluate the integrated profile functions of ϕ_m , ϕ_h , and ϕ_q (instead of the vertical gradients of these functions) because the measured profiles show smaller noise fluctuations than the gradients derived from them. Following Jimenéz et al. (2012) and the definition in Panofsky (1963), the profile functions can be written as

$$u(z) = \frac{u_*}{k} \left[\ln \left(\frac{z-d}{z_0} \right) - \psi_m \left(\frac{z-d}{L} \right) + \psi_m \left(\frac{z_0}{L} \right) \right] \quad (5)$$

$$\theta(z) = \frac{\theta_*}{k} \left[\ln \left(\frac{z-d}{z_0} \right) - \psi_h \left(\frac{z-d}{L} \right) + \psi_h \left(\frac{z_0}{L} \right) \right] + \theta_s \quad (6)$$

$$q(z) = \frac{q_*}{k} \left[\ln \left(\frac{z-d}{z_0} \right) - \psi_q \left(\frac{z-d}{L} \right) + \psi_q \left(\frac{z_0}{L} \right) \right] + q_s \quad (7)$$

with $u(z)$, $\theta(z)$, and $q(z)$ the profiles of wind, potential temperature, and humidity, z_0 the roughness length, d the displacement height, θ_s the surface temperature, q_s the surface moisture, and the temperature and humidity scale as

$$\theta_* = -\frac{H_0}{\rho c_p u_*} = -\frac{(\overline{w' \theta'})_s}{u_*} \quad (8)$$

$$q_* = -\frac{Q_0}{L_e \rho u_*} = -\frac{(\overline{w' q'})_{s_0}}{u_*}. \quad (9)$$

The formulation of the humidity profile $q(z)$ in Eq. (7) is given similar as the temperature profile with q_* instead of θ_* as the similarity functions for heat and moisture are formulated in the same way (Dyer and Hicks 1970). The same equation for humidity profiles was applied by Eichinger et al. (2000) but given with a sign mistake in their publication (Eq. (1)).

The integrated similarity functions $\psi_{m,h,q}$ are defined according to the atmospheric stability which is classified by the bulk-Richardson number (Jiménez et al., 2012)

$$R_b = \frac{g}{\theta_a} z \frac{\theta_{va} - \theta_{vs}}{U^2}. \quad (10)$$

with θ_{va} and θ_{vs} the virtual potential temperature in the atmosphere at 10 m altitude and at the surface, respectively. For unstable atmospheric conditions with free convection R_b becomes < 0 , which is true for our case. Thus, we use the $\psi_{m,h,q}$ functions (Paulson, 1970; Dyer, 1974; Beljaars and Holtslag, 1991; Jiménez et al., 2012) as

$$\psi_m = 2 \ln\left(\frac{1+x}{2}\right) + \ln\left(\frac{1+x^2}{2}\right) - 2 \tan^{-1}(x) + \frac{\pi}{2} \quad (11)$$

$$\psi_{h,q} = 2 \ln\left(\frac{1+x^2}{2}\right) \quad (12)$$

with

$$x = \left[1 - 16 \left(\frac{z}{L}\right)\right]^{1/4}. \quad (13)$$

While Eichinger et al. (2000) only measured the humidity profile with Raman lidar, they needed to include additional surface measurements of u_* and the L calculation to retrieve the latent surface heat flux. Having the combination of measured lidar profiles of $u(z)$, $\theta(z)$, and $q(z)$ allows to solve the three equations (5)-(7) to get u_* , H_0 and Q_0 without additional information. To find a consistent solution for the surface fluxes, we use a combined nonlinear least-square optimization method for the observed profiles and Eq. (5)-(7), namely the Levenberg-Marquart method, which varies smoothly between the extremes of the steepest descent method and the inverse-Hessian method (Press et al., 2007). For nonlinear least square problems with multiple local minima it is appropriate to use the best available estimates of the desired parameters as initial start values. We found that this method works very well and converges to reasonable parameters if plausible starting values for the parameters can be guessed. (Gavin, 2020). For our study we use the Matlab tools of Gavin (2020) and start the iteration with local measurements of the EB station. This seems to meet the appropriate local minimum to achieve reasonable results. However, if EB data are not available, using just the lidar data and climatological estimates for the first guess will produce reasonable values for the fluxes.

4 Lidar surface layer profiles

We use measurements from IOP 11 on 23 Aug 2017 from the time periods 1840-1930, 1940-2030, and 2040-2140 UTC to demonstrate our procedure described in Sect. 3. Each lidar system performed SL scans as described in Sect. 2.1 to obtain virtual tower profiles. Here, to demonstrate the method, we focus on TWR 2 because we have the best sampling with all lidars. All three DLs scanned over TWR 2. TWR 1 was challenging with respect to the range averaging applied to the q and T data because of near-field overlap limitations in the nearest couple of hundreds of meters close to the lidars. At TWR 2 the range average for the temperature calculation is acceptable which needs to be increased for the larger distances at TWR 3 and 4 to keep the noise level acceptably low.

The vertical humidity field at 1905 UTC along the main scan direction measured with the WVDIAL is shown in Figure 2a for the range 400 to 2500 m. The plot shows a single scan and thus the instantaneous humidity field. In Figure 2b the LOS wind along the main scan direction of one DALEK scan at the same time is shown. The plots show negative elevation angles, which were required to capture the landscape with lower altitude with respect to the lidar location at the ARM SGP central facility. The first 400 m close to the DIAL are affected by the non-full overlap of the laser beam and the field-of-view of the telescope and, thus, cannot be used. Due to the strong backscattering return signal of the ground and of obstacles, the humidity data are disturbed over certain ranges close to the surface. This affected range smears out according to the selected SaGo window range of the derivative applied in the WV calculation. The data shows little distortion close to the surface around ranges of 900, 1200, 1600, and 2300 m distance due to obstacles which were hit. These obstacles were filtered in the raw data and the gaps filled by interpolation to continue the data retrieval over these areas close to the ground. Nevertheless, the data points close to the surface are omitted in the further analysis because they show non-realistic artifacts. For wind and temperature data these range bins are filtered out. However, the obstacles and the ground return were used to calibrate the elevation angles with respect to the surface level. The zero level of the height scale in Figure 2 is given with respect to the altitude where the lidars were located at the ARM SGP central facilities. This shows lower terrain in the area of interest of around 15 m in altitude.

The scan plane was kept over the EB stations throughout the LAFE campaign. On 23 Aug 2017, the wind was roughly oriented along this scan direction as determined with the intersecting DL scans over the EB stations. While an RHI of Doppler wind data shows only the LOS component in general, here, the data of the RHI (Figure 2b) are thus very similar to the full horizontal wind velocity.

Both humidity and LOS wind show vertical structures with higher and lower values over the whole measured height range. As seen in consecutive scans, these mesoscale structures move through the area of investigation and may indicate vertical mixing.

Figure 3 shows the 50-minute mean humidity field averaged over 42 consecutive scans between 1840 and 1930 UTC to extract the virtual tower profiles (dashed lines). The omitted data are shaded and not used for further analysis. The humidity field shows almost constant values with a slight increase towards the surface. The resulting profiles for that 50-minute period of horizontal wind, absolute humidity, and potential temperature at TWR 2 are shown in

Figure 4a.

Figure 4b and c give the profiles for the following 50-minute periods, 1940-2030 UTC and 2040-2130 UTC. The plots show a height range from the land surface up to 100 m above ground level (agl) which cover the SL assuming that the SL is about ten percent as thick as the ABL. Surface measurements from the EB tower at 2 m and 10 m are shown in addition to the lidar observation.

The wind profile of the first case shows low wind at the surface and increases up to 3.5 ms^{-1} at a height of 100 m agl. The lowest data point was retrieved at 8 m agl. There is a small difference between lidar and EB measurements, which may be due to a different sampling volume of the lidars. The EB measurement gives a point measurement whereas lidar apply range averaging over the capture range of $\pm 100\text{m}$ around the tower. The second case show similar wind values and the third case stronger winds up to 4.8 ms^{-1} at a height of 100 m agl.

The humidity profile in

Figure 4a shows values close to 10 gm^{-3} in the SL with increasing values towards the surface as expected. This is consistent with a moistening SL from the surface due to evapotranspiration. The lowest measurement point of the lidar is at 13 m and can be extended

with EB measurements at 10 and 2.5 m towards the surface. During the following period similar humidity was present while during the last period the humidity decreased to 9.5 gm^{-3} . This drying is due to advection which shifted the whole profile to lower values and is also indicated by an increased horizontal wind. The EB data indicate an increase between the 2 and 10 m level of about 1 gm^{-3} .

The potential temperature is almost constant at around 301 K in all three cases. In general, the relative measurement uncertainty for temperature measurements is much larger than for wind and humidity. However, the profile agrees very well with the 2 m and 10 m EB measurements which also show no large gradient.

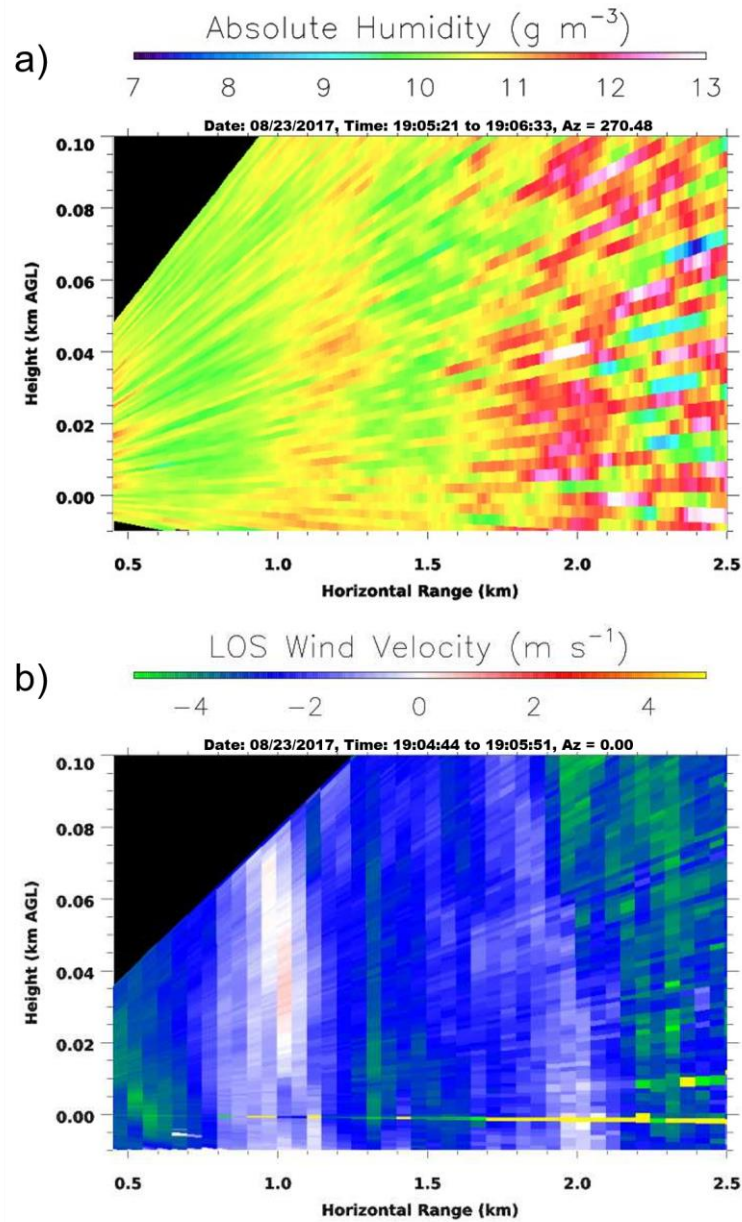


Figure 2. Vertical cross-section along the main scan direction to the northeast. a) Absolute humidity field measured with the WVDIAL and b) line-of-sight wind measured with the Doppler lidar DALEK. The data are of scans made during about 50 s at about 1905 UTC with scan speeds of 0.1°s^{-1} and 0.08°s^{-1} , respectively. The height scale shows height with respect to the lidar site near the ARM SGP central facility.

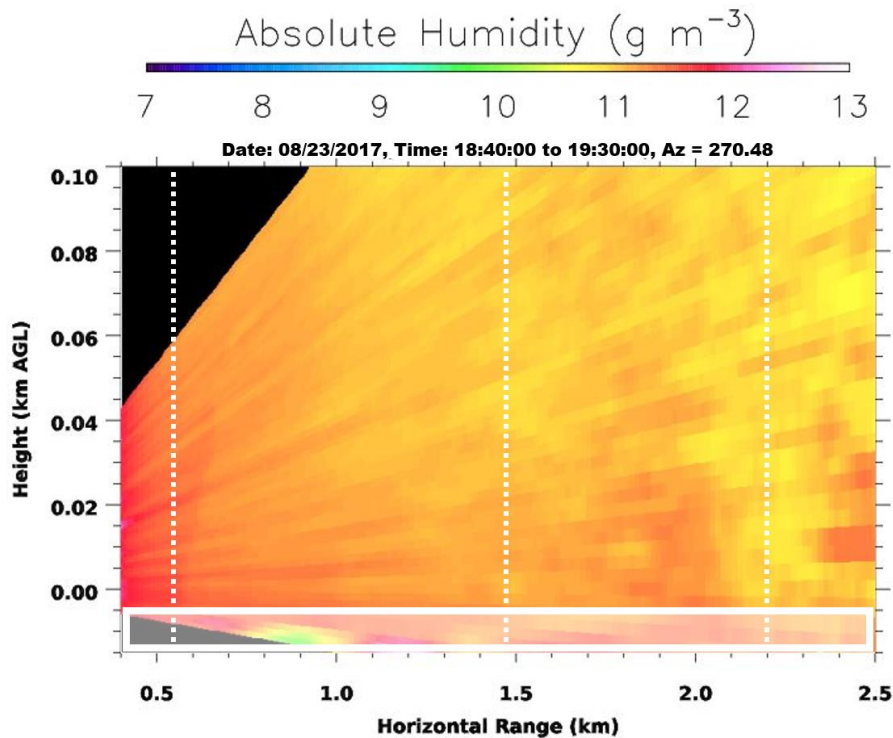


Figure 3. The mean humidity field along the main scan direction to the northeast averaged over the 50-minute period between 1840 and 1930 UTC is shown. This mean contains 42 consecutive scans. The dashed lines indicate the position of the virtual towers. A bipolar structure close to the surface is due to corrections of strong return signals from the ground and obstacles (white box). These data are not used in the analysis.

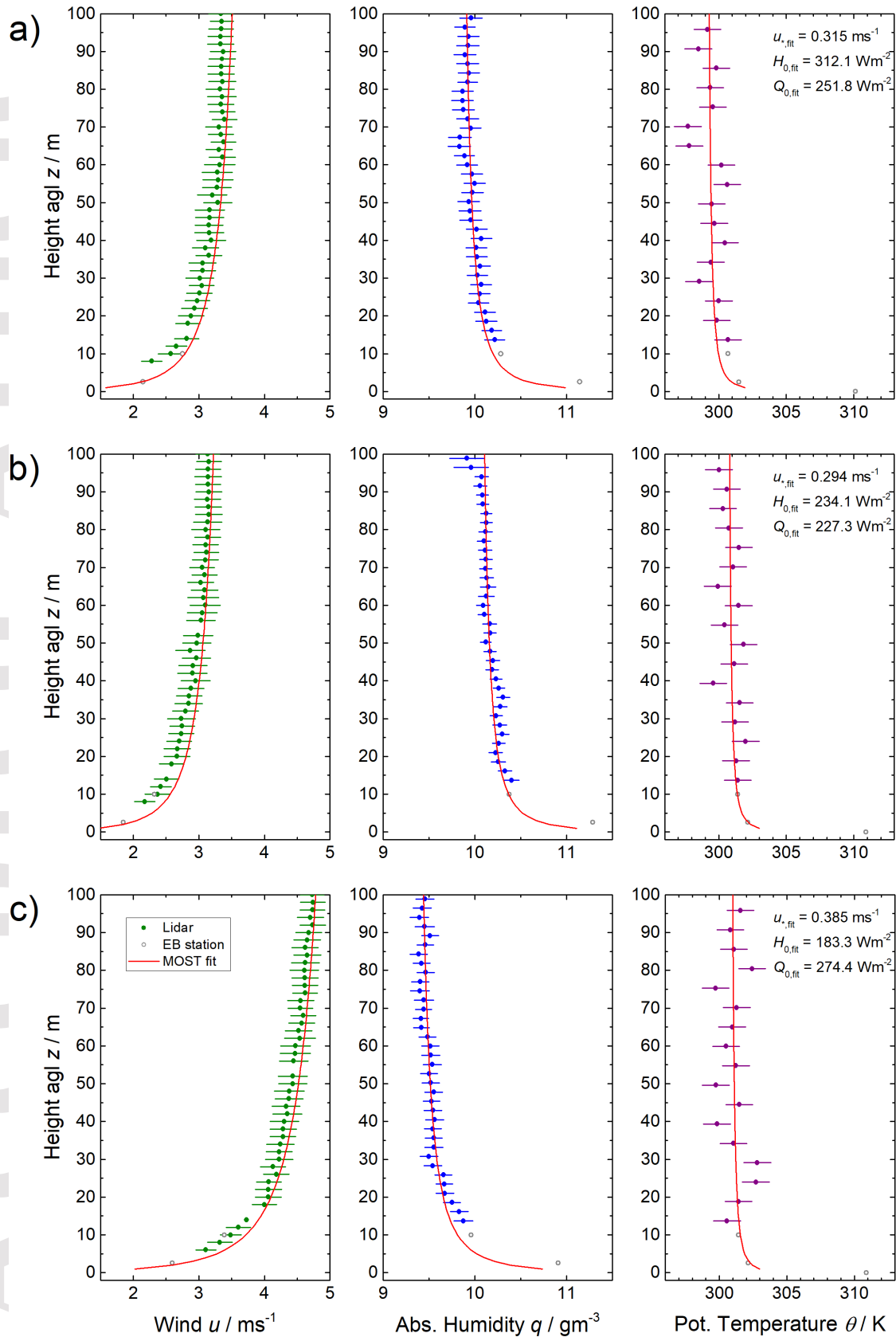


Figure 4. Virtual tower profiles from the lidar measurements extracted at TWR 2 for horizontal wind, absolute humidity, and potential temperature from 23 Aug 2017 for the time periods a) 1840-1930, b) 1940-2030, and c) 2040-2130 UTC. Lidar data are plotted with filled dots, the error bars are the error of the mean, surface values from the EB station were plotted with open circles and the MOST fit was plotted as red line. EB station data are independent and were not used for the MOST fit. Nevertheless, the extrapolated fit profiles are very close to the EB data at 2 and 10 m. The flux data and u_* which result from the optimization method are also given (see next section and Table 2 for more details).

5 Comparison of Lidar profiles with MOST profiles

We can apply Eq. (5)-(7) to determine the latent and sensible surface heat fluxes. As explained in Sect. 3, we use the Levenberg-Marquart iteration method to fit MOST profiles to the virtual tower profiles of wind, humidity and temperature from Sect. 4. Our intention is to use u_* , H_0 , and Q_0 as main fit parameters and to find a consistent solution to solve all three equations. The fits were realized with the Levenberg-Marquardt algorithm for nonlinear least squares curve-fitting problems and the Matlab routines of Gavin (2020). As start values for the iterations we took the EB measurements as first guess. A fully consistent optimization including all three profiles in one optimization cycle did not converge. Thus, fits were individually realized for wind, humidity, and temperature profiles sequentially. For that, different numbers of fit parameters were selected. First, we calculated the fit for the wind profile and included the friction velocity u_* and an offset value u_s at the land surface as additional fit parameter. The resulting values were then used to calculate the fit for the humidity profile leaving Q_0 and q_s to be varied. Finally, to fit the MOST temperature profile to the lidar profile only H_0 and θ_s were used as fit parameters to find the best fit. The displacement d was set to zero for all fits. The results for all fit parameters are given in Table 2. Parameters which were varied in the optimization iteration are given with uncertainties. Values without an uncertainty were kept constant during the iteration.

In

Figure 4 the fitted profiles are plotted in red. For heights above 20 m agl the fits and the lidar agree within the error bars. Below, the fitted MOST profiles continue with a smooth gradient down to the surface. The profiles show that the largest change occurs in the lowest 20 m agl. The DL profile of case 1 shows its gradient higher above ground than the EB measurements which results in a certain displacement of the MOST profile. However, the MOST profile reproduces the EB data points at 2 and 10 m even though the fit was done without the EB data. The different measurement volume of the lidar data maybe especially critical close to the surface. The friction velocity was retrieved from the fit to $0.315 \text{ ms}^{-1} \pm 0.019 \text{ ms}^{-1}$, to $0.294 \text{ ms}^{-1} \pm 0.017 \text{ ms}^{-1}$, and to $0.385 \text{ ms}^{-1} \pm 0.012 \text{ ms}^{-1}$ and showed for all cases slightly larger values than measured at the EB tower. The wind offset was determined to be zero for all cases.

The MOST profiles of humidity reproduced the lidar profiles almost completely within the sampling errors except of the lowest data points. It continues down to the surface following the EB data points. Also here, the largest gradient is close to the surface but could be derived from the lidar profile. The latent heat flux was estimated to 251.8, 227.3, and 274.4 Wm^{-2} with uncertainties of 33.7, 42.4, and 31.1 Wm^{-2} , respectively. All fluxes are higher than measured at the EB station but they agree with a lower flux for case 2 and an increase for case 3. The Q_0 of the EB station given in Table 2 are measured at 2.5 m agl, additional measurements at 10 m show larger values and also larger values with up to a daily maximum latent heat flux of 350 Wm^{-2} were observed at the ARM SGP CF. The increase of Q_0 of case 3 results from the drying SL and an increased humidity gradient.

From the fit of the temperature profile the sensible heat flux and the surface temperature were determined. The data points show larger scatter than the wind and moisture profiles. However, the fits delivered reasonable H_0 and θ_s estimates. The surface fluxes of case 1 and 2 are 312.1 and 234.1 Wm^{-2} , respectively, which are higher than observed with the EB station but followed the trend of decreasing heat flux. For case 3 the estimation from the lidar profile and the EB measurement agree. However, the uncertainties are very large which indicate no robust results. This means a larger change of the fit parameter by little changes of the input data. The surface temperature values of 305.7, 306.0, and 305.1 K with uncertainties of 12.0, 9.3, and 10.7 K are lower than the 310 K observed with the EB station but within the uncertainties. The MOST profiles follow the lidar profiles within the uncertainties using all other parameters from the wind and humidity fit.

In conclusion, the MOST fits both reproduce the lidar profiles and also agree with the EB data points close to the surface. For all three quantities, the height range close to the surface of the lowest 10-15 m show the steepest gradient, which was not fully covered by the lidar profiles due to challenges with the non-uniform height of the terrain at the SGP site. To measure profiles closer to the surface using scanning lidar systems, it would be advantageous to select a measurement site having a flat or uphill terrain along the scan direction to avoid disturbance from ground return signals, especially for the WVDIAL. Nonetheless, the estimated friction velocity and sensible surface fluxes from the fits show realistic values. The derived friction velocity and heat fluxes are higher than what was measured with the EB station but can be

realistic as higher fluxes up to 350 Wm^{-2} were observed at the ARM SGP CF , which is 1.5 km away from TWR 2. Due to the large spatial variability of the sensible heat flux observations around the SGP site, there is no resilient evaluation of the total surface heat fluxes possible. The overestimation of both heat fluxes might also be due to the initial values of the fit parameters for which we think the EB data are the most reasonable guesses.

As seen in Figure 4, temperature lidar data with higher precision (smaller statistical uncertainty) would be very valuable. It is noteworthy in this context, that the Raman lidar used in this study had been developed more than 10 years before LAPE (Radlach et al, 2008). In the meantime the laser and receiver technology has it made possible to build similar systems with much better performance (Lange et al., 2019).

Table 2. Fit parameter values used for calculating the MOST profiles in

Figure 4. The EB values were used as start values for the iteration. Values without uncertainty were set constant for the optimization.

Fit Parameter		1840-1930 UTC	1940-2030 UTC	2040-2130 UTC
u^* (ms^{-1})		0.315 ± 0.019	0.294 ± 0.017	0.385 ± 0.012
	EB	0.264	0.235	0.323
H_0 (Wm^{-2})		312.1 ± 841.5	234.1 ± 589.2	183.3 ± 629.4
	EB	219.0	197.0	184.5
Q_0 (Wm^{-2})		251.8 ± 33.7	227.3 ± 42.4	274.4 ± 31.1
	EB	227.0	206.0	213.0
z_0 (m)	EB	0.11	0.11	0.11
u_s (ms^{-1})		0.0 ± 0.3	0.0 ± 0.3	0.0 ± 0.2
q_s (gm^{-3})		12.4 ± 0.3	12.4 ± 0.4	12.1 ± 0.3
θ_s (K)		305.7 ± 12.0	306.0 ± 9.3	305.1 ± 10.7
	EB	310.1	310.9	310.4
θ_0 (K)	EB	300.8	301.4	302.3
ρ_{air} (gm^{-3})	EB	1.1414	1.1388	1.1351

6 Summary and Outlook

Surface layer profiles of wind, humidity, and temperature were collected during LAFE in August 2017 to investigate land-atmosphere interactions. For the first time, these three quantities were simultaneously measured in the SL with scanning lidar systems. Their profiles in the lowest 100 m above ground level were captured over an agricultural landscape and averaged over 50-minute periods. The lidar profiles were used to estimate friction velocities and surface fluxes of sensible and latent heat following MOST. The estimated similarity functions for momentum, heat and moisture were fitted to the lidar profiles iteratively.

This new method is discussed and illustrated with three 50-minutes time periods from 23 Aug 2017. In these periods, the CBL was fully developed. The fits of the MOST profiles agree with the lidar profiles and resulted in realistic fit values of friction velocity, sensible and latent surface heat fluxes, and surface values of wind, absolute humidity and potential temperature. For the friction velocity and both heat fluxes we get higher estimates than observed with the EB station but the temporal behavior is similar. We conclude that the estimates obtained from the lidar scans in combination with the MOST fits are reasonable given both the large heterogeneity in the experimental area and the sampling differences between the two techniques. Additional research is needed to investigate the dependence of the solution on the initial guess and the impact of plausible start values for the nonlinear least square curve-fitting.

The achieved height resolution of a few meters was sufficient to resolve the SL profiles, so that the sampling concept itself can be recommended for future campaigns. The steepest gradients are present in the lowest 5 to 15 m above the canopy top, i.e., in the height region that was unfortunately not well sampled by all lidars during LAFE. In particular, the WVDIAL humidity measurements were disturbed by ground return peaks from higher vegetation, power-line poles, wires etc. in the path of the laser beam. Such disturbances should be avoided in future campaigns. Since the diameter of the outgoing laser beam of the lidars has a diameter of only about 2 m at 2 km distance (divergence of 1 mrad) it is easily possible to slightly adapt the scan direction and avoid hard targets in the lidar beam. Also with a slightly changed azimuth scan direction by a few meters, the data collected close to the surface over a mean of about 1 hour will be representative for the SL above the surfaces of interest. Thus, higher priority can be given to

avoid systematic errors and near-surface hard targets. Furthermore, the position of the lidars was slightly uphill and about 10 m higher than the canopy top of the vegetation below the lidar scans during LAFE. This resulted in surface returns for all scan profiles with negative elevation. Consequently, a lidar site at the altitude of the canopy top or slightly below is preferable.

The LAFE dataset contains a large suite of further measurement periods. The analysis of their statistics, their relation to different periods of LAFE and their diurnal cycle is beyond the scope of this paper and will be discussed elsewhere. Furthermore, we plan more measurements at the Land-Atmosphere Feedback Observatory (LAFO) at the University of Hohenheim, which will consider the aforementioned aspects regarding the scan geometry and make also use of recent advances in scanning lidar technology. More research on the most suitable MOST similarity functions will be possible with such extended data sets, also regarding the influence of surface heterogeneities on L-A feedback processes which is considered paramount for improving the representation of L-A processes in numerical weather predictions models and climate models.

Appendix: Vertical resolution of lidar measurements

The vertical resolution Δz of lidar measurements is limited by two factors: 1) the elevation scan speed ϖ combined with the temporal resolution of the measurements Δt

$$\Delta z_1 = R \Delta \alpha = R \varpi \Delta t$$

and 2) the vertical projection of the gate width Δr

$$\Delta z_2 = \Delta r \sin \alpha.$$

For a virtual tower at distance x the range R for a given elevation angle α is

$$R = x \cos \alpha$$

and the corresponding height z is

$$z = R \sin \alpha.$$

In the SL with small elevation angles, effect 1 is nearly constant with respect to height z at a given distance x while effect 2 depends to a larger degree on the elevation angle α (and hence z). The

resulting resolution is the sum of both effects while effect 1 dominates at lower heights and limits the resolution, whereas at larger heights effect 2 manifests as an increase of the covered height range.

Acknowledgments, Samples, and Data

LAFE was funded by the DOE ARM program, NASA, and NOAA in the United States as well as the BMBF in Germany via the HD(CP)² project. The ARM Atmospheric System Research (ASR) program provided partial support for this analysis via grant DE-SC0014375. The NOAA Atmospheric Science for Renewable Energy (ASRE) program also provided some support for this analysis. We acknowledge the support of LAFE by Aditya Choululkar, Timothy A. Bonin, Simon Metzendorf, and Shravan Kumar Muppa.

The LAFE dataset is freely available through the ARM Data Discovery portal (<https://adc.arm.gov/discovery/>).

References

- Andreae, M. O., O. C. Acevedo, A. Araùjo, P. Artaxo, C. G. G. Barbosa, H. M. J. Barbosa, J. Brito, S. Carbone, X. Chi, B. B. L. Cintra, N. F. da Silva, N. L. Dias, C. Q. Dias-Júnior, F. Ditas, R. Ditz, A. F. L. Godoi, R. H. M. Godoi, M. Heimann, T. Hoffmann, J. Kesselmeier, T. Könemann, M. L. Krüger, J. V. Lavric, A. O. Manzi, A. P. Lopes, D. L. Martins, E. F. Mikhailov, D. Moran-Zuloaga, B. W. Nelson, A. C. Nölscher, D. Santos Nogueira, M. T. F. Piedade, C. Pöhlker, U. Pöschl, C. A. Quesada, L. V. Rizzo, C.-U. Ro, N. Ruckteschler, L. D. A. Sá, M. de Oliveira Sá, C. B. Sales, R. M. N. dos Santos, J. Saturno, J. Schöngart, M. Sörgel, C. M. de Souza, R. A. F. de Souza, H. Su, N. Targhetta, J. Tóta, I. Trebsa, S. Trumbore, A. van Eijck, D. Walter, Z. Wang, B. Weber, J. Williams, J. Winderlich, F. Wittmann, S. Wolff, and A. M. Yáñez-Serrano (2015) The Amazon Tall Tower Observatory (ATTO): overview of pilot measurements on ecosystem ecology, meteorology, trace gases, and aerosols, *Atmos. Chem. Phys.*, 15, 10723–10776, doi:10.5194/acp-15-10723-2015
- Butterworth, B. J., Desai, A. R., Metzger, S., Townsend, P. A., Schwartz, M. D., Petty, G. W., Mauder, M., Vogelmann, H., Andresen, C. G., Augustine, T. J., Bertram, T. H., Brown, W. O. J., Buban, M., Cleary, P., Durden, D. J., Florian, C. R., Iglinski, T. J., Kruger, E. L., Lantz, K., Lee, T. R., Meyers, T. P., Mineau, J. K., Olson, E. R., Oncley, S. P., Paleri, S., Pertzborn, R. A., Pettersen, C., Plummer, D. M., Riihimaki, L. D., Guzman, E. R., Sedlar, J., Smith, E. N., Speidel, J., Stoy, P. C., Sührling, M., Thom, J. E., Turner, D. D., Vermeuel, M. P., Wagner, T. J., Wang, Z., Wanner, L., White, L. D., Wilczak, J. M., Wright, D. B., & Zheng, T. (2021), Connecting Land–Atmosphere Interactions to Surface Heterogeneity in CHEESEHEAD19, *Bulletin of the American Meteorological Society*, 102(2), E421–E445, doi:10.1175/BAMS-D-19-0346.1

- Behrendt, A., (2005), Temperature measurements with Lidar. In: C. Weitkamp (Ed.), Lidar: Range-Resolved Optical Remote Sensing of the Atmosphere, Springer Series in Optical Sciences 102, 273-305, ISBN: 0-387-40075-3, Springer, New York, doi:10.1007/0-387-25101-4_10
- Behrendt, A., V. Wulfmeyer, E. Hammann, S. K. Muppa, and S. Pal (2015), Profiles of second- to fourth-order moments of turbulent temperature fluctuations in the convective boundary layer: first measurements with rotational Raman lidar. *Atmos. Chem. Phys.* 15, 5485-5500, doi:10.5194/acp-15-5485-2015
- Behrendt, A., V. Wulfmeyer, C. Senff, S. K. Muppa, F. Späth, D. Lange, N. Kalthoff, and A. Wieser (2020), Observation of sensible and latent heat flux profiles with lidar. *Atmos. Meas. Tech.* 13, 3221-3233, doi:10.5194/amt-13-3221-2020
- Beljaars, A. C. M., and A. A. M. Holtslag (1991), Flux Parameterization over Land Surfaces for Atmospheric Models, *J. Appl. Meteorol. Clim.*, 30(3), 327-341, doi:10.1175/1520-0450(1991)030<0327:FPOLSF>2.0.CO;2
- Berger, B. W., K.J. Davis, C. Yi, P.S. Bakwin, C.L. Zhao (2001) Long-Term Carbon Dioxide Fluxes from a Very Tall Tower in a Northern Forest: Flux Measurement Methodology, *Journal of Atmospheric and Oceanic Technology*, 18(4), 529-542, doi:10.1175/1520-0426(2001)018<0529:LTCDFD>2.0.CO;2
- Blumberg, W. G., D.D. Turner, U. Löhnert, and S. Castleberry (2015) Ground-Based Temperature and Humidity Profiling Using Spectral Infrared and Microwave Observations. Part II: Actual Retrieval Performance in Clear-Sky and Cloudy Conditions, *J. Appl. Meteorol. Clim.*, 54(11), 2305-2319, doi:10.1175/JAMC-D-15-0005.1
- Bodini, N., Lundquist, J. K., and Optis, M. (2020), Can machine learning improve the model representation of turbulent kinetic energy dissipation rate in the boundary layer for complex terrain?, *Geosci. Model Dev.*, 13, 4271–4285, doi:10.5194/gmd-13-4271-2020
- Calhoun, R., Heap, R., Princevac, M., Newsom, R., Fernando, H., and Ligon, D. (2006), Virtual towers using coherent Doppler lidar during the Joint Urban 2003 dispersion experiment, *J. Appl. Meteorol. Clim.*, 45, 1116–1126, doi:10.1175/JAM2391.1
- Choukulkar, A., Brewer, W. A., Sandberg, S. P., Weickmann, A., Bonin, T. A., Hardesty, R. M., Lundquist, J. K., Delgado, R., Iungo, G. V., Ashton, R., Debnath, M., Bianco, L., Wilczak, J. M., Oncley, S., and Wolfe, D. (2017), Evaluation of Single and Multiple Doppler Lidar Techniques to Measure Complex Flow during the XPIA Field Campaign, *Atmos. Meas. Tech.*, 10, 247–264, doi:10.5194/amt-10-247-2017
- Cooney, J. (1972). Measurement of Atmospheric Temperature Profiles by Raman Backscatter, *J. Appl. Meteorol. Clim.*, 11(1), 108-112, doi:10.1175/1520-0450(1972)011<0108:MOATPB>2.0.CO;2
- Dyer, A.J. (1974), A review of flux-profile relationships, *Bound.-Lay. Meteor.*, 7, 363–372, doi:10.1007/BF00240838
- Dyer, A. J., and B. B. Hicks (1970), Flux-gradient relationships in the constant flux layer. *Quart. J. Roy. Meteor. Soc.*, 96, 715–721, doi:10.1002/qj.49709641012

- Eichinger, W., D. Cooper, J. Kao, L. C. Chen, L. Hipps, J. Prueger (2000), Estimation of spatially distributed latent heat flux over complex terrain from Raman lidar, *Agricultural and Forst Meteorology* 105, 145-159
- Foken, T. (2006), 50 Years of the Monin–Obukhov Similarity Theory, *Bound.-Lay. Meteor.*, 119, 431–447, doi:10.1007/s10546-006-9048-6
- Froidevaux, M., Higgins, C. W., Simeonov, V., Ristori, P., Pardyjak, E., Serikov, I., Calhoun, R., van den Bergh, H., and Parlange, M. B. (2012), A Raman lidar to measure water vapor in the atmospheric boundary layer, *Adv. Water Resour.*, 51, 345–356, doi:10.1016/j.advwatres.2012.04.008
- Gavin, H.P. (2020), The Levenberg-Marquardt algorithm for nonlinear least squares curve-fitting problems, <https://people.duke.edu/~hpgavin/ce281/lm.pdf>
- Hammann, E. and A. Behrendt (2015), Parametrization of optimum filter passbands for rotational Raman temperature measurements. *Opt. Express* 23(24), 30767-30782, doi:10.1364/OE.23.030767
- Hammann, E., A. Behrendt, F. Le Mounier, and V. Wulfmeyer (2015), Temperature profiling of the atmospheric boundary layer with rotational Raman lidar during the HD(CP)2 Observational doi:10.5194/acp-15-2867-2015 Prototype Experiment. *Atmos. Chem. Phys.* 15, 2867-2881
- Ismail, S. and Browell, E. V. (1989) Airborne and spaceborne lidar measurements of water vapor profiles: a sensitivity analysis, *Appl. Opt.*, 28, 3603–3615, doi:10.1364/AO.28.003603
- Jiménez, P. A., J. Dudhia, J. F. González-Rouco, J. Navarro, J. P. Montávez, and E. García-Bustamante (2012), A revised scheme for the WRF surface layer formulation. *Mon. Weather Rev.*, 140(3), 898-918, doi:10.1175/MWR-D-11-00056.1
- Kiese, R., Fersch, B., Baessler, C., Brosy, C., Butterbach-Bahl, K., Chwala, C., Dannenmann, M., Fu, J., Gasche, R., Grote, R., Jahn, C., Klatt, J., Kunstmann, H., Mauder, M., Rödiger, T., Smiatek, G., Soltani, M., Steinbrecher, R., Völksch, I., Werhahn, J., Wolf, B., Zeeman, M. and Schmid, H. (2018), The TERENO Pre-Alpine Observatory: Integrating Meteorological, Hydrological, and Biogeochemical Measurements and Modeling. *Vadose Zone Journal*, 17: 1-17 180060, doi:10.2136/vzj2018.03.0060
- Lagerquist, R., D.D. Turner, I. Ebert-Uphoff, J. Stewart, and V. Hagerty, 2021: Using deep learning to emulate and accelerate a radiative transfer model. *J. Atmos. Oceanic Tech.*, 38, 1673-1696, doi:10.1175/JTECH-D-21-0007.1.
- Lange, D., A. Behrendt, and V. Wulfmeyer (2019), Compact operational tropospheric water vapor and temperature Raman Lidar with turbulence resolution. *Geophys. Res. Lett.*, 46(24), 14844-14853, doi:10.1029/2019GL085774
- Lee, T. R., & Buban, M. (2020). Evaluation of Monin–Obukhov and Bulk Richardson Parameterizations for Surface–Atmosphere Exchange, *Journal of Applied Meteorology and Climatology*, 59(6), 1091-1107, DOI:10.1175/JAMC-D-19-0057.1
- Lee, T., M. Buban, E. Dumas, and C. Baker (2019), On the Use of Rotary-Wing Aircraft to Sample Near-Surface Thermodynamic Fields: Results from Recent Field Campaigns, *Sensors*, 19(1), 10, doi:10.3390/s19010010

- Lee, X., W. Massman, B.E. Law (2004), Handbook of micrometeorology. A guide to surface flux measurements and Analysis. – Kluwer, Dordrecht.
- Lenschow, D. H., Wulfmeyer, V., and Senff, C. (2000) Measuring second-through fourth-order moments in noisy data, *J. Atmos. Oceanic. Tech.*, 17, 1330–1347, doi:10.1175/1520-0426(2000)017<1330:MSTFOM>2.0.CO;2
- Mauder, M., T. Foken, and J. Cuxart (2020), Surface-Energy-Balance Closure over Land: A Review, *Bound.-Lay. Meteor.*, 177, 395–426, doi:10.1007/s10546-020-00529-6
- Metzendorf, S. (2018), 10 W-Average-Power single-frequency Ti:sapphire Laser with tuning agility – A breakthrough in high-resolution 3D water-vapor measurement. Dissertation, University of Hohenheim, Institute for Physics and Meteorology, <http://opus.uni-hohenheim.de/volltexte/2019/1558/>
- Monin, A. S., and A. M. Obukhov, (1954), *Tr. Akad. Nauk SSSR Geofiz. Inst.*, 24, 163–187.
- Muppa, S. K., A. Behrendt, F. Späth, V. Wulfmeyer, S. Metzendorf, and A. Riede (2016), Turbulent humidity fluctuations in the convective boundary layer: Case studies using water vapour differential absorption lidar measurements. *Bound.-Lay. Meteor.* 158, 43-66, doi:10.1007/s10546-015-0078-9
- Neisser, J., W. Adam, F. Beyrich, U. Leiterer, H. Steinhagen, (2002) Atmospheric boundary layer monitoring at the Meteorological Observatory Lindenberg as a part of the "Lindenberg Column": Facilities and selected results, *Meteorol. Z.*, 11, 4, 241-253, doi: 10.1127/0941-2948/2002/0011-0241
- Obukhov, A. M. (1971), Turbulence in an atmosphere with a nonuniform temperature, *Bound.-Lay. Meteor.*, 2, 7–29, doi:10.1007/BF00718085
- Panofsky H.A. (1963), Determination of Stress from Wind and Temperature Measurements, *Quart. J. Roy. Meteorol. Soc.*, 89, 85–94, doi:10.1002/qj.49708937906
- Paulson, C. A. (1970), The Mathematical Representation of Wind Speed and Temperature Profiles in the Unstable Atmospheric Surface Layer, *J. Meteor. Clim.*, 9(6), 857-861, doi:10.1175/1520-0450(1970)009<0857:TMROWS>2.0.CO;2
- Press, W.H., S.A. Teukolsky, W.T. Vetterling, B.P. Flannery (2007), Numerical recipes: the art of scientific computing – 2nd ed., Cambridge University Press, ISBN 978-0-521-88068-8, <http://numerical.recipes>
- Radlach, M., A. Behrendt, and V. Wulfmeyer (2008), Scanning rotational Raman lidar at 355 nm for the measurement of tropospheric temperature fields. *Atmos. Chem. Phys.* 8, 159-169, doi:10.5194/acp-8-159-2008
- Röckmann T., S. Eyer, C. van der Veen, M.E. Popa, B. Tuzson, G. Monteil, S. Houweling, E. Harris, D. Brunner, H. Fischer, G. Zazzeri, D. Lowry, E.G. Nisbet, W.A. Brand, J.M. Necki, L. Emmenegger, and J. Mohn (2016), In situ observations of the isotopic composition of methane at the Cabauw tall tower site, *Atmos. Chem. Phys.*, 16, 10469–10487, doi:10.5194/acp-16-10469-2016
- Santanello Jr, J. A., P. A. Dirmeyer, C. R. Ferguson, K. L. Findell, A. B. Tawfik, A. Berg, M. Ek, P. Gentile, B. P. Guillod, C. van Heerwaarden, J. Roundy, and V. Wulfmeyer (2018),

- Land–Atmosphere Interactions: The LoCo Perspective. *B. Am. Meteorol. Soc.* 99(6), 1253-1272, doi:10.1175/BAMS-D-17-0001.1
- Späth, F., S. Metzendorf, A. Behrendt, H.-D. Wizemann, G. Wagner, and V. Wulfmeyer (2013), Online/offline injection seeding system with high frequency-stability and low crosstalk for water vapor DIAL. *Opt. Commun.* 309, 37-43, doi:10.1016/j.optcom.2013.07.003
- Späth, F., A. Behrendt, S. K. Muppa, S. Metzendorf, A. Riede, and V. Wulfmeyer (2016), 3D water vapor field in the atmospheric boundary layer observed with scanning differential absorption lidar. *Atmos. Meas. Tech.* 9, 1701-1720, doi:10.5194/amt-9-1701-2016
- Sisterson, D.L., R.A. Pepler, T.S. Cress, P.J. Lamb, and D.D. Turner (2016) The ARM Southern Great Plains (SGP) site. *The Atmospheric Radiation Measurement (ARM) program: The first 20 years*. Meteor. Monograph, 57, Amer. Meteor. Soc., 6.1-6.14, doi:10.1175/AMSMONOGRAPHS-D-16-0004.1.
- Turner, D. D., Ferrare, R. A., Brasseur, L. A. H., Feltz, W. F., & Tooman, T. P. (2002), Automated Retrievals of Water Vapor and Aerosol Profiles from an Operational Raman Lidar, *Journal of Atmospheric and Oceanic Technology*, 19(1), 37-50, doi:10.1175/1520-0426(2002)019<0037:AROWVA>2.0.CO;2
- Turner, D. D., and U. Löhnert (2021), Ground-based temperature and humidity profiling: combining active and passive remote sensors, *Atmos. Meas. Tech.*, 14, 3033–3048, doi:10.5194/amt-14-3033-2021
- Wagner, G., V. Wulfmeyer, F. Späth, A. Behrendt, and M. Schiller (2013) Performance and specifications of a pulsed high-power single-frequency Ti:Sapphire laser for water-vapor differential absorption lidar. *Appl. Optics* 52(11), 2454-2469, doi:10.1364/AO.52.002454
- Wagner, T. J., Klein, P. M., & Turner, D. D. (2019), A New Generation of Ground-Based Mobile Platforms for Active and Passive Profiling of the Boundary Layer, *Bulletin of the American Meteorological Society*, 100(1), 137-153, doi:10.1175/BAMS-D-17-0165.1
- Wizemann, H.-D., J. Ingwersen, P. Högy, K. Warrach-Sagi, T. Streck, and V. Wulfmeyer (2015), Three year observations of water vapor and energy fluxes over agricultural crops in two regional climates of Southwest, Germany. *Meteorol. Z.* 24(1), 39-59, doi:10.1127/metz/2014/0618
- Wolfe, D.E. and R.J. Latatits (2018) Boulder Atmospheric Observatory: 1977–2016: The End of an Era and Lessons Learned, *B. Am. Meteorol. Soc.*, 99(7), 1345-1358, doi:10.1175/BAMS-D-17-0054.1
- Wulfmeyer, V. (1999), Investigations of humidity skewness and variance profiles in the convective boundary layer and comparison of the latter with large eddy simulation results. *J. Atmos. Sci.* 56(8), 1077-1087, doi:10.1175/1520-0469(1999)056<1077:IOHSAV>2.0.CO;2
- Wulfmeyer, V., D. D. Turner, S. Pal, and E. Wagner (2010), Can water vapour Raman lidar resolve profiles of turbulent variables in the convective boundary layer? *Bound.-Lay. Meteorol.* 136, 253-284, doi:10.1007/s10546-010-9494-z
- Wulfmeyer, V., S. K. Muppa, A. Behrendt, E. Hammann, F. Späth, Z. Sorbjan, D. D. Turner, and R. M. Hardesty (2016), Determination of convective boundary layer entrainment fluxes,

dissipation rates, and the molecular destruction of variances: Theoretical description and a strategy for its confirmation with a novel lidar system synergy. *J. Atmos. Sci.* 73(2), 667-692, doi:10.1175/JAS-D-14-0392.1

Wulfmeyer, V. , D.D. Turner, B. Baker, R. Banta, A. Behrendt, T. Bonin, W. A. Brewer, M. Buban, A. Choukulkar, E. Dumas, R M. Hardesty, T. Heus, J. Ingwersen, D. Lange, T. R. Lee, S. Metzendorf, S. K. Muppa, T. Meyers, R. Newsom, M. Osman, S. Raasch, J. Santanello, C. Senff, F. Späth, T. Wagner, and T. Weckwerth (2018), A New research approach for observing and characterizing Land-Atmosphere Feedback. *B. Am. Meteorol. Soc.*, 99(8), 1639-1667, doi:10.1175/BAMS-D-17-0009.1

Yuval, J. and P.A. O’Gorman (2020), Stable machine-learning parameterization of subgrid processes for climate modeling at a range of resolutions. *Nat Commun* **11**, 3295, doi:10.1038/s41467-020-17142-3